International Journal of Mechanical Sciences 328 (2026) 112017

Contents lists available at ScienceDirect

International Journal of Mechanical Sciences

journal homepage: www.elsevier.com/locate/ijmecsci

Micromechanical insights into tensile deformation of epoxy-infiltrated hierarchical nanoporous copper

Tim Fischer [a,*], Norbert Huber [a,b]

[a] Institute of Materials Physics and Technology, Hamburg University of Technology, Eißendorfer Straße 42, Hamburg, D-21073, Germany
[b] Bundesanstalt für Materialforschung und -prüfung (BAM), Unter den Eichen 87, Berlin, D-12205, Germany

ARTICLE INFO

Keywords:
Nanoporous metals
Metal–polymer composites
Micromechanical modeling
Hierarchical nanoporous copper
Epoxy infiltration
Plastic strain localization

ABSTRACT

Hierarchical nanoporous metals infiltrated with polymers offer enhanced tensile stability while retaining functional porosity, yet their micromechanical deformation mechanisms remain insufficiently understood. Here, a micromechanics-based finite element framework is developed for epoxy-filled hierarchical nanoporous copper (HNPCu) based on experimentally derived structural parameters. The hierarchical ligament architecture across two structural levels as well as selective epoxy infiltration are explicitly resolved, enabling phase-specific analysis of local stress and strain evolution. The predicted tensile response is validated against experiments for different Cu solid fractions ($0.1 \leq \varphi \leq 0.2$), and the experimentally observed trends are well reproduced using idealized microstructures. Epoxy infiltration markedly reduces plastic strain localization within the Cu network, leading to a more homogeneous deformation state compared to epoxy-free HNPCu. At the macroscopic level, the tensile response remains largely unaffected by epoxy infiltration at small strains, with differences emerging only at larger deformation. Strain localization is predicted both within Cu ligaments and near Cu–epoxy interfaces, consistent with experimentally observed microcrack formation along phase boundaries and inside the Cu network. These findings provide micromechanical insight into hierarchy-assisted deformation in polymer-infiltrated nanoporous metals and establish a basis for microstructure-guided design of mechanically robust hierarchical materials.

1. Introduction

Nanoporous metals prepared by dealloying have attracted considerable attention due to their large specific surface area, open porosity, and tunable ligament morphology [1–3]. These structural characteristics enable a broad range of applications exploiting the large internal surface area and open porosity of nanoporous metals. In catalysis, nanoporous gold has been used for selective gas-phase oxidative coupling of methanol [4], while nanoporous copper offers tunable porosity for surface-enhanced Raman spectroscopy [5]. The same surface sensitivity enables actuation: charge-induced reversible strain [6], surface-chemistry-driven actuation in nanoporous gold [7], electrically tunable strength and flow stress [8], and bulk actuation behavior [9] have all been demonstrated, with hierarchical bulk nanoporous Cu specifically showing enhanced electrochemical actuation response [10]. For energy storage and conversion, nanoporous metal/oxide hybrids serve as supercapacitor electrodes [11], dealloyed 3D copper structures act as dendrite-free lithium anode current collectors [12], lamellar nanoporous metal/intermetallic heterostructures regulate dendrite-free zinc electrodeposition [13], and dealloying more broadly enables electrochemical energy conversion and storage applications [14]. Beyond these functional roles, nanoporous metals also offer tunable electronic structure–property relationships [15], and recent work has extended hierarchical architectures to bulk nanoporous Cu with improved mechanical processing routes [16,17], including skeletal design strategies inspired by traditional architectural principles [18], motivating the general formation and property review of nanoporous metals by alloy corrosion [2]. Beyond their functional properties, the mechanical stability of nanoporous metals is essential for maintaining structural integrity during fabrication, assembly, and service.

Despite their high strength, nanoporous metals are notoriously brittle under bending and tensile loading. This strength originates from a pronounced “smaller is stronger” size effect at the nanoscale: twinned nanoporous gold exhibits enhanced tensile strength via twin-boundary strengthening [19], flaw-free nanoporous Ni ligaments approach theoretical tensile strength [20], and systematic scaling laws relate stiffness and strength to ligament size across hierarchical network nanomaterials [21]. Similar size-dependence has been reported for nanoporous Au [22], for the role of monolayer surface oxides in raising flow stress at small ligament sizes [23], and for compression-induced deformation of nanoporous gold nanoparticles [24], with related scaling

* Corresponding author.
E-mail address: tim.fischer@tuhh.de (T. Fischer).

https://doi.org/10.1016/j.ijmecsci.2026.112017
Received 9 May 2026; Received in revised form 8 August 2026; Accepted 15 August 2026
Available online 24 August 2026

behavior established for the Poisson's ratio of hierarchical nanoscale networks [25]. This brittle behavior is characteristic of both non-hierarchical and hierarchical nanoporous metals, as deformation is governed by stress concentration and failure within the interconnected ligament network, manifesting macroscopically as brittle fracture in nanoporous-gold-polymer composites [26,27], epoxy-infiltrated hierarchical nanoporous Cu [28], and tension–compression asymmetric plasticity in nanoporous gold [29].

Local ligament fracture can trigger stress redistribution and cascading failure once the load exceeds the strength of adjacent ligaments, leading to abrupt macroscopic fracture. This ductile-to-brittle transition was first characterized for random porous Au [30] and later linked to microscopic failure mechanisms [31] and lattice coherency during deformation [32]. Micro- and millimeter-scale testing has further quantified tensile and compressive failure of bulk nanoporous gold [33–36], while atomistic simulations have examined plastic deformation in nanoscale gold single crystals and open-celled nanoporous gold [37]. More recently, native-oxide-shelled nanoporous aluminum was shown to combine light weight, strength, and stability [38], and capillary-shrinkage-induced crack healing via cold welding was identified as a mechanism for controlling the ductile-to-brittle transition in nanoporous gold [39]. Several strategies have been proposed to improve ductility, including structural coarsening and twin engineering [19], exploiting tension–compression asymmetry [29], controlling the ductile–brittle transition through relative density [30,35], and introducing weak grain boundaries in dealloyed porous Fe alloys [40]. Polymer infiltration represents a further route to enhanced mechanical stability, either by converting open pores into closed voids (as in nanoporous-gold-polymer composites [26,27] and monolithic nanoporous Cu composites [41]) or through dispersed nanovoid strengthening [42], with the mechanical contribution of the polymer phase itself isolated via dedicated testing protocols [43]. However, these strategies typically compromise the intrinsic high surface area or open architecture required for functional applications, limiting their practical implementation. In contrast, partially polymer-infiltrated hierarchical nanoporous metals offer a promising route to enhance mechanical stability while maintaining a substantial portion of the functional porosity, as demonstrated for hierarchical network nanomaterials [21] and epoxy-infiltrated hierarchical nanoporous Cu specifically [28]. Polymer or ceramic infiltration to stabilize metallic or cellular networks is an established strategy more broadly across lightweight metallic cellular materials [44], as illustrated by resin-infiltrated interpenetrating-phase composites [45,46], elastomer-infiltrated auxetic lattices [47], and functionally graded spinodal nanoarchitected ceramics [48].

To better understand and predict the mechanical behavior of nanoporous metal–polymer composites, computational approaches have been widely employed at different length scales. Atomistic simulations such as molecular dynamics have provided valuable insight into deformation mechanisms at the ligament scale, revealing anomalous compliance and early yielding behavior in nanoporous gold [49] and scaling laws governing stiffness and strength across hierarchical network architectures [21]. However, their limited accessible length scales make explicit modeling of metal–polymer composites challenging.

Consequently, continuum approaches such as finite element (FE) and micromechanical models have been widely used to study nanoporous metal–polymer systems. Griffiths et al. developed composite models capturing how polymer infiltration strengthens nanoporous gold while enabling actuation-driven polymer motion [50] and identified fracture mechanisms in polymer-impregnated nanoporous gold [51]; Bargmann et al. presented a computational framework for the mechanical behavior of gold-polymer nanocomposites [52]; Li et al. analyzed the compressive deformation behavior of nanoporous-gold-based composites via FE analysis [53]; and Gnegel et al. numerically investigated polymer-coated nanoporous gold [54]. These studies have primarily focused on non-hierarchical microstructures with homogeneous polymer infiltration, providing insight into load transfer, stress redistribution, and fracture mechanisms, but do not resolve hierarchical ligament architecture. Recent data-driven models represent among the first attempts to describe the elasto-plastic behavior of hierarchical nanoporous metals, including multiaxial yield-behavior prediction [55] and physics-informed recurrent neural networks for hierarchical FE modeling [56], although explicit representation of hierarchical geometry and polymer infiltration effects remains absent from these approaches. Recent large-scale structural–mechanical property datasets for nanoporous networks derived from FE simulations [57] and correlative multiscale microscopy-modeling approaches revealing nanoscale plasticity in metallic nanosponges [58] further support data-driven and scale-bridging strategies for nanoporous metal deformation. Beyond nanoporous metals specifically, hierarchical lattice architectures are increasingly explored for tailoring mechanical performance through hierarchical pentamode-like unit cells [59], gradient bionic lattice designs [60], and plate-TPMS hierarchical lattices [61], underscoring the broader relevance of explicitly resolved hierarchical geometry for mechanical design. Accordingly, the coupling between explicitly resolved hierarchical architecture and selective polymer infiltration across multiple structural levels remains unexplored.

In this work, a micromechanics-based FE framework is developed for epoxy-filled hierarchical nanoporous copper (HNPCu) that explicitly resolves the lower- and upper-level ligament networks as well as selective polymer infiltration at the upper hierarchy. The model is constructed from experimentally derived structural parameters, enabling phase-resolved analysis of the mechanical response under tensile loading. By comparing epoxy-free and epoxy-infiltrated configurations across different solid fractions, the framework provides a quantitative basis for assessing the mechanical role of hierarchy and polymer infiltration, with model predictions evaluated against experimentally observed mechanical behavior and damage features. The remainder of this paper is organized as follows. Section 2 summarizes the experimental background and structural parameters underlying the model. Section 3 describes the construction of the hierarchical FE model, the constitutive assumptions, and the boundary conditions. Section 4 presents the macroscopic and phase-resolved micromechanical results, including validation against experimental data and analysis of stress and strain partitioning between the Cu and epoxy phases. Section 5 concludes the paper and outlines implications for microstructure-guided design of hierarchical nanoporous metal–polymer composites.

2. Materials and experimental background

To establish a physically grounded micromechanical model and ensure meaningful comparison with experiments, the present simulations are based on the experimentally characterized epoxy–HNPCu system reported recently in [28]. The key structural parameters and mechanical observations relevant for model construction and validation are summarized below.

HNPCu was fabricated via a three-step process involving selective phase etching of a dual-phase Mn–Cu precursor, epoxy infiltration of the resulting microporous γ-Mn(Cu) framework, and subsequent electrochemical dealloying to generate a nanoporous Cu network [28]. During this process, epoxy selectively infiltrates the larger pore channels formed at the upper structural level, while the nanoscale porosity generated during dealloying remains open. The resulting material therefore exhibits a bicontinuous hierarchical architecture composed of a microscale ligament network containing an embedded nanoscale ligament network [18,21,25,62,63]. The hierarchical structure is characterized by two distinct length scales, as illustrated schematically in Fig. 1. The upper level is defined by a mean ligament diameter l_2 in the range of approximately 1.5 to 2.1 μm and a corresponding solid fraction φ_2, determined by the volume fraction of the γ-Mn(Cu) phase

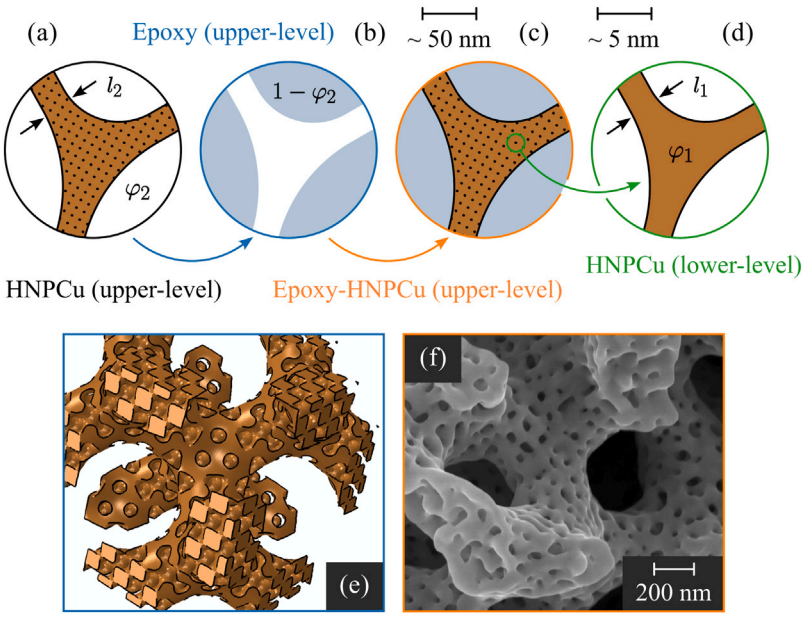

Fig. 1. Hierarchical nanoporous copper (HNPCu) architecture and selective epoxy infiltration. **(a)** Upper hierarchical level without epoxy, defined by ligament size l_2 and solid fraction φ_2. **(b)** Epoxy occupying the upper-level pore network with solid fraction $1-\varphi_2$, and **(c)** resulting composite structure after selective infiltration. **(d)** Lower hierarchical level without epoxy, defined by ligament size l_1 and solid fraction φ_1; epoxy percolates at the upper hierarchy, while the lower-level nanoscale porosity remains open. **(e)** Corresponding upper-level ligament junction in the FE model geometry, and **(f)** SEM image of hierarchical nanoporous gold adapted from [62], under CC BY license, exhibiting an upper-level solid fraction of $\varphi_2 = 0.52$, lower-level solid fraction of $\varphi_1 = 0.38$, and ligament sizes $l_2 = 320$ nm, $l_1 = 48$ nm.

in the precursor. Epoxy occupies the interconnected pore network at this scale (Fig. 1b–c). The lower level, generated by electrochemical dealloying, consists of Cu nanoligaments with a mean diameter $l_1 \approx 42$ nm and a relative density φ_1 between 0.45 and 0.49 (Fig. 1d). Importantly, the lower-level nanoscale porosity remains open, while epoxy percolates only at the upper hierarchy. The overall solid fraction of the hierarchical Cu structure is given by $\varphi = \varphi_1\varphi_2$, and was varied in the range $0.1 \leq \varphi \leq 0.2$ by adjusting the precursor composition [28]. These experimentally determined parameters form the geometric basis of the FE model.

Quasi-static tensile tests were performed on dog-bone-shaped specimens at a nominal strain rate of 10^{-4} 1/s [28]. In-situ tensile experiments were conducted inside a scanning electron microscope (SEM), enabling direct observation of deformation and damage evolution. Strain fields were quantified using digital image correlation (DIC). Microcrack formation was observed both along Cu–epoxy interfaces and within the Cu ligament network, providing direct experimental benchmarks for validating the predicted stress–strain response and strain localization patterns.

3. Simulation methods

This section describes the construction of the hierarchical micromechanical FE model. Section 3.1 introduces the geometric representation of the hierarchical ligament network and the associated structural parameters, while Section 3.2 details the constitutive material models, interface assumptions, and boundary conditions applied in the simulations. The term "micromechanical" is used here in the established sense of continuum micromechanics of heterogeneous materials (i.e., explicit resolution of distinct constituent phases and structural levels within a continuum FE framework to predict phase-resolved local fields and their relation to the macroscopic response [50,52,54]) rather than atomistic-scale mechanisms. This distinction is made explicit to avoid overstating the resolution at which deformation mechanisms are captured.

3.1. Hierarchical model and structural parameters

The hierarchical epoxy–HNPCu FE models are constructed to explicitly resolve the upper- and lower-level ligament networks while preserving experimentally derived structural parameters. The geometry is idealized using a periodic diamond lattice-type unit cell with smoothly curved ligament junctions, reproducing the bicontinuous morphology and nodal connectivity characteristic of nanoporous metals [64–67]. A qualitative comparison between an upper-level ligament junction in the hierarchical FE model and an experimentally observed hierarchical nanoporous structure is shown in Fig. 1e–f. The FE geometry (Fig. 1e) captures the essential morphological features of ligament junctions, including curvature and connectivity, while remaining computationally tractable, closely resembling the experimental microstructure (Fig. 1f). The use of an idealized, periodic diamond-lattice geometry rather than an experimentally reconstructed 3D microstructure is a deliberate methodological choice, consistent with established practice in continuum micromechanical modeling of nanoporous metals [50,52,64,67]. Prior work comparing randomized and periodic ligament geometries showed that randomization softens the response and suppresses transverse contraction, while periodic diamond-lattice unit cells already capture the fundamental deformation mechanisms [64], supporting their use as an efficient basis for more complex, hierarchical microstructures. Periodicity enables systematic, controlled variation of hierarchy level and infiltration fraction without confounding these effects with sample-specific structural disorder. This trades quantitative representation of any single real microstructure for general, comparative conclusions across configurations, at the cost of not capturing local stress and strain amplification associated with structural disorder, which is expected to further increase the intensity of strain localization relative to the present predictions (Section 4.2). Extending the framework to experimentally reconstructed, statistically representative volumes is a natural direction for future work.

The hierarchical architecture is generated in three steps (Fig. 2). First, a single-scale diamond lattice unit cell is created to represent the upper hierarchy, with an upper-level solid fraction φ_2 (Fig. 2a, e, m).

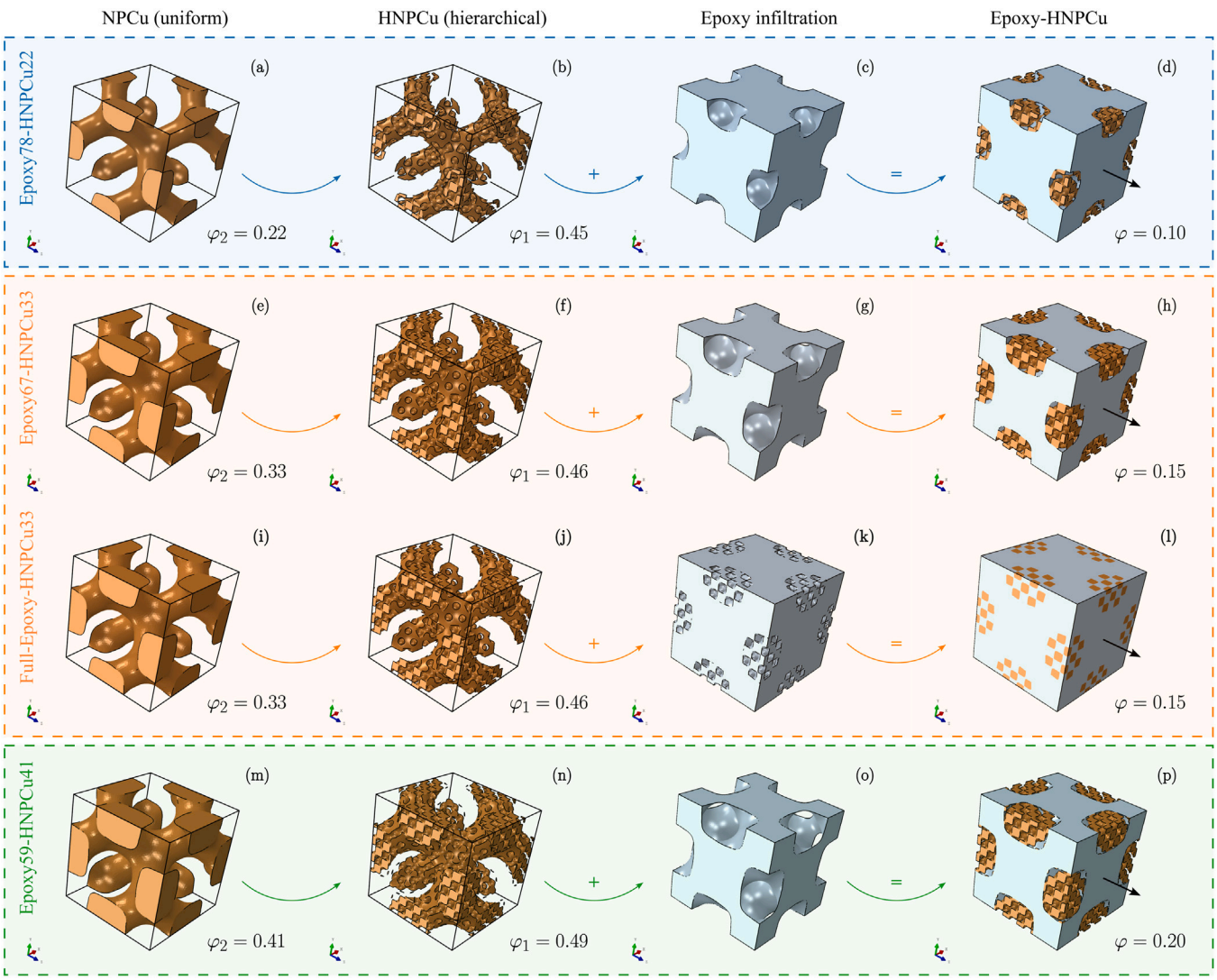

Fig. 2. Construction of the hierarchical epoxy–HNPCu FE models. **(a, e, i, m)** Diamond lattice-type unit cell with curved ligament junctions forming a uniform single-scale structure, **(b, f, j, n)** corresponding hierarchical structure, and **(c, g, k, o)** selective epoxy infiltration at the upper hierarchy. **(d, h, l, p)** Final epoxy–HNPCu composite models used for simulations. The Epoxy78–HNPCu22 **(a–d)**, Epoxy67–HNPCu33 and pore-free Full-Epoxy67–HNPCu33 **(e–l)**, and Epoxy59–HNPCu41 **(m–p)** models are defined by total solid fractions of 0.10 ($\varphi_2 = 0.22$, $\varphi_1 = 0.45$), 0.15 ($\varphi_2 = 0.33$, $\varphi_1 = 0.46$), and 0.20 ($\varphi_2 = 0.41$, $\varphi_1 = 0.49$), respectively.

Second, the unit cell is scaled to the lower ligament level and its solid fraction independently adjusted to φ_1, then periodically replicated to form a self-similar two-level structure. This geometric scaling defines the hierarchy ratio l_2/l_1 between the characteristic ligament lengths of the two structural levels. Each upper-level ligament is replaced by a nanoscale porous substructure, resulting in a fully resolved hierarchical network (Fig. 2b, f, n). Third, selective epoxy infiltration is applied at the upper hierarchy by filling the corresponding pore network while preserving the nanoscale porosity within the lower-level ligaments (Fig. 2c, g, o). The resulting composite configurations used for simulation are shown in Fig. 2d, h, p. Three primary composite configurations are considered, corresponding to total Cu solid fractions φ of 0.10, 0.15, and 0.20. These are denoted as Epoxy78–HNPCu22 (Fig. 2a–d), Epoxy67–HNPCu33 (Fig. 2e–h), and Epoxy59–HNPCu41 (Fig. 2m–p), reflecting the respective epoxy and upper-level Cu volume fractions. The associated upper- and lower-level solid fractions are $(\varphi_2, \varphi_1) = (0.22, 0.45)$, $(0.33, 0.46)$, and $(0.41, 0.49)$, respectively. For each configuration, a corresponding epoxy-free hierarchical Cu model is constructed to isolate the effect of selective infiltration. In addition, pore-free fully infiltrated reference models (Full-Epoxy67–HNPCu33, Fig. 2i–l) are generated by completely filling the hierarchical pore network with epoxy. These models serve to distinguish the influence of retained nanoscale porosity from that of full polymer embedding. Collectively, they enable a systematic comparison between (i) hierarchical Cu without epoxy, (ii) selectively infiltrated hierarchical composites, and (iii) fully infiltrated pore-free reference structures at identical overall Cu contents.

The experimentally derived structural parameters of the three main composite configurations are summarized in Table 1. Again, the lower hierarchy is defined by the ligament size l_1 and solid fraction φ_1, whereas the upper hierarchy is characterized by l_2, φ_2, and the epoxy volume fraction $\varphi_{\text{epoxy}} = 1 - \varphi_2$. The overall Cu solid fraction follows as $\varphi = \varphi_1\varphi_2$. The experimentally measured hierarchy ratios l_2/l_1 (>35) exceed those accessible in fully resolved FE simulations. To ensure numerical feasibility while retaining the governing deformation mechanisms, the hierarchy ratios are geometrically downscaled to 4.0, 4.9, and 5.4 for the three configurations, preserving the experimentally observed increasing trend between the structures. This downscaling reduces the number of hierarchical junction generations relative to experiment and is expected to underestimate the intensity of strain

Table 1
Structural parameters of the hierarchical epoxy–HNPCu models. The lower hierarchy is characterized by φ_1 and l_1, the upper hierarchy by φ_2, φ_{epoxy}, and l_2. The overall solid fraction φ and the experimental hierarchy ratio l_2/l_1 are reported. For numerical feasibility, the experimental hierarchy ratios are geometrically downscaled to 4.0, 4.9, and 5.4 for the three configurations. Structural parameters are provided by the experimental reference work [28] and adapted for the computational model.

Composite model	φ_1	l_1, nm	φ_2	φ_{epoxy}	l_2, µm	φ	l_2/l_1
Epoxy78–HNPCu22	0.45	42	0.22	0.78	1.5	0.10	35.7
Epoxy67–HNPCu33	0.46	43	0.33	0.67	1.6	0.15	37.2
Epoxy59–HNPCu41	0.49	42	0.41	0.59	2.1	0.20	50.0

Table 2
Calibrated and literature-based material constants used in the FE simulations. σ_0, σ_∞, and b are the Voce hardening parameters for Cu, calibrated against the Epoxy67–HNPCu33 configuration. Epoxy is modeled as linear elastic without plasticity.

Parameter	Cu	Epoxy
E, MPa	130 000	1
ν	0.34	0.49
σ_0, MPa	20	–
σ_∞, MPa	80	–
b	50	–

localization, since a larger hierarchy ratio increases the number of weak-link-type junction sites available for strain concentration (Section 4.2). The absolute magnitude of predicted local stresses and strains should therefore be interpreted as a lower-bound estimate of the true multiscale localization behavior, while the relative trends between configurations (which govern the comparative conclusions drawn in this study) are expected to be more robust to this approximation, since the downscaling is applied consistently across all configurations. All other structural parameters are adapted from the experimental reference work and provide the quantitative basis for the computational models. The discretization consists of up to two million linear tetrahedral elements with full integration, depending on the solid fraction and resulting geometric complexity of the hierarchical network.

3.2. Material model and boundary conditions

Cu ligaments are modeled as an isotropic elastoplastic material with nonlinear isotropic hardening. The elastic response of Cu is characterized by Young's modulus $E_{Cu} = 130$ GPa and Poisson's ratio $\nu_{Cu} = 0.34$, agreeing with standard literature values for polycrystalline Cu. Plastic flow follows a von Mises yield criterion with a Voce-type isotropic hardening law. The flow stress σ evolves with accumulated equivalent plastic strain ε^{p}_{eq} according to $\sigma = \sigma_0 + (\sigma_\infty - \sigma_0)[1 - \exp(-b\varepsilon^{p}_{eq})]$, where $\sigma_0 = 20$ MPa is the initial yield stress, $\sigma_\infty = 80$ MPa is the saturation stress, and $b = 50$ controls the hardening rate. The hardening parameters were identified by fitting the model predictions to the experimental tensile response of the intermediate epoxy–HNPCu configuration (Epoxy67–HNPCu33) reported in [28] and were subsequently used consistently across all simulations. Predictive capability of the calibrated model is assessed independently against the two remaining, non-calibrated configurations (Section 4.1). The epoxy phase is modeled as nearly incompressible linear elastic material without plasticity ($E_{epoxy} = 1$ MPa, $\nu_{epoxy} = 0.49$). These properties are taken directly from tensile tests on epoxy monoliths reported in the experimental reference study and reflect the highly compliant, rubber-like behavior of the EF80 flexible resin system (Easy Composites), which cures into a soft thermoset [28]. The assumption of linear elastic epoxy behavior is consistent with the strain range experienced by the polymer phase: bulk epoxy monoliths of the same resin system deform elastically up to strains exceeding 50% [28], while the predicted local maximum principal strain in the epoxy remains below approximately 38% at 2% macroscopic strain (Section 4.2). A hyperelastic description would mainly affect the absolute magnitude of local epoxy stress, not phase partitioning: given the already large Cu–epoxy stress contrast (>600), even a several-fold change would not alter the conclusion that epoxy carries a negligible fraction of the macroscopic load. The more relevant sensitivity lies in the epoxy's confinement effect on Cu deformation stability, consistent with the modulus sensitivity analysis (Section 4.2). Perfect bonding is assumed at all Cu–epoxy interfaces, and no interfacial decohesion is included in the present simulations. This assumption enables isolation of the intrinsic micromechanical deformation mechanisms arising from hierarchical architecture and selective infiltration. While this assumption precludes explicit prediction of interfacial decohesion and crack propagation, it allows direct assessment of whether stress and strain concentrations naturally develop at the Cu–epoxy interface from elastic mismatch and hierarchical geometry alone. Predicted sites of maximum principal strain in the epoxy phase coincide with the Cu–epoxy interface and agree with experimentally observed interfacial microcracks (Section 4.2), indicating that the model already captures the mechanical origin of interfacial damage initiation, even without predicting subsequent crack growth. The epoxy-modulus sensitivity analysis (Section 4.2) shows that locally reducing epoxy stiffness measurably reduces macroscopic stress, consistent with reduced confinement. By analogy, progressive interfacial decohesion is expected to accelerate rather than delay strain localization, suggesting the perfect-bonding assumption likely overestimates macroscopic ductility. The extensive Cu–epoxy interface network makes cohesive-zone modeling itself numerically challenging, requiring dedicated future simulations. All simulations were performed using the implicit solver of Abaqus (Dassault Systèmes) within a geometrically nonlinear large-deformation framework. The calibrated material constants used in all simulations are summarized in Table 2.

Uniaxial tensile loading is applied using grip-type boundary conditions, consistent with the loading conditions used in the reference experiments. The reference face is fully constrained by prescribing zero displacement in all spatial directions. On the loading face, a prescribed displacement is imposed in the tensile direction, while transverse displacements are constrained to zero. The global stress–strain response is obtained from the reaction forces at the loading face normalized by the initial cross-sectional area, and the macroscopic strain is computed from the applied displacement relative to the initial unit cell length.

Continuum micromechanical modeling is widely used across metallic and composite cellular materials, including creep of porous sintered silver via Fourier-transform-based homogenization [68], elastic stability of orthotropic titanium foams [69], compression of aluminum foam composites [70,71], and interfacial bonding in aluminum foam [72]. Related composite-level approaches include low-rank strain approximation in two-phase composites [73], nano-interfacial and agglomeration effects in hybrid composites [74], dissolvable micromechanics modeling [75], and micromechanical characterization of additively manufactured architected structures [76]. Similar strategies have also been applied to functionally graded Al–SiC composites [77], machine-learning-guided metal matrix composite design [78], graphene foam modeling [79], high-strain-rate nanotwinned alloys [80], and hierarchical plate-lattice metamaterials [81].

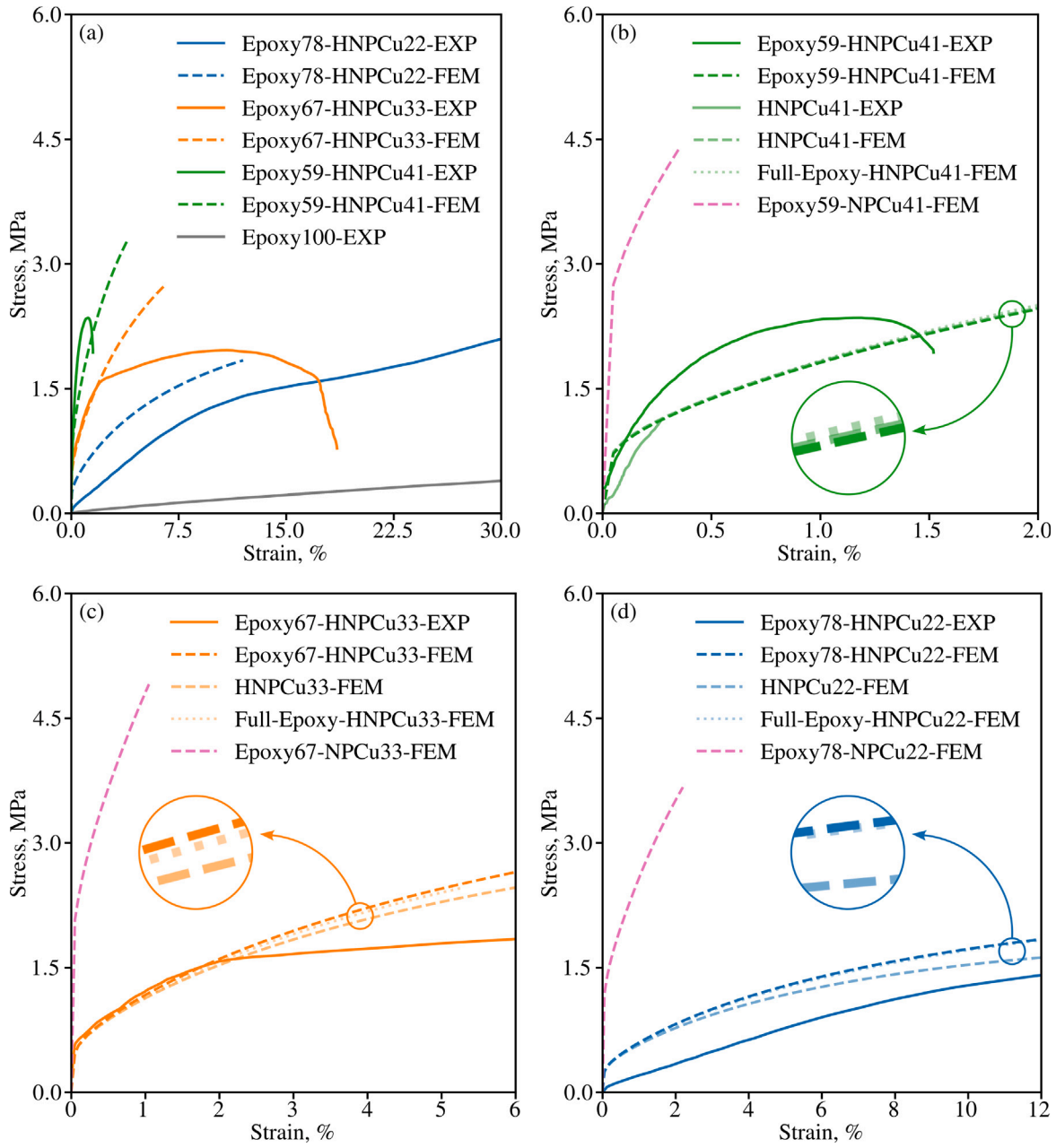

Fig. 3. Tensile stress–strain behavior of hierarchical epoxy–HNPCu composites, including FE predictions and experimental results [28]. **(a)** Comparison of predictions and experimental measurements for Epoxy78–HNPCu22, Epoxy67–HNPCu33, and Epoxy59–HNPCu41. The experimental bulk epoxy response is also depicted (Epoxy100). **(b–d)** Predictions for each hierarchical epoxy–HNPCu configuration compared with epoxy-free HNPCu, experimental results, pore-free full-epoxy models (epoxy on both hierarchy levels), and single-scale epoxy–NPCu models without hierarchy.

4. Results and discussion

This section presents the predicted mechanical response of the hierarchical epoxy–HNPCu composites. Section 4.1 compares the macroscopic tensile stress–strain behavior of the different composite configurations with experimental measurements, while Section 4.2 provides a phase-resolved micromechanical analysis of local stress and strain fields to elucidate the deformation mechanisms underlying the macroscopic response.

4.1. Macroscopic response of hierarchical epoxy–HNPCu composites

The macroscopic tensile stress–strain responses of the hierarchical epoxy–HNPCu composites are shown in Fig. 3, together with the corresponding micromechanical FE predictions. Fig. 3a compares the simulated and experimentally measured responses for the three selectively infiltrated configurations: Epoxy78–HNPCu22 ($\varphi = 0.10$), Epoxy67–HNPCu33 ($\varphi = 0.15$), and Epoxy59–HNPCu41 ($\varphi = 0.20$). The measured tensile response of monolithic epoxy (Epoxy100) is also included for reference.

All selectively infiltrated hierarchical composites exhibit pronounced plastic deformation and strain hardening, and the simulations reproduce the experimentally observed trends across the investigated solid fractions. Quantitatively, the elastic modulus E and 0.2%-offset yield stress σ_y predicted by the model agree closely with experiment for the calibration configuration (Epoxy67–HNPCu33), while differing more markedly for the two non-calibrated configurations (Table 3): E and σ_y are overpredicted at low φ and underpredicted

Table 3
Comparison of experimentally measured and FE-predicted elastic modulus E and 0.2%-offset yield stress σ_y. Epoxy67–HNPCu33 was used for calibration. The other configurations are independent predictions.

Composite model	E_{EXP}, MPa	E_{FEM}, MPa	$\sigma_{y,EXP}$, MPa	$\sigma_{y,FEM}$, MPa
Epoxy78–HNPCu22	49.6	134.9	0.191	0.472
Epoxy67–HNPCu33	263.1	250.0	0.869	0.913
Epoxy59–HNPCu41	502.6	378.0	2.157	1.430

at high φ. This trend is consistent with the power-law dependence of stiffness and strength on solid fraction typical of nanoporous metals, whereby small geometric deviations between model and experiment, amplified by the hierarchy-ratio downscaling (Table 1), translate into larger relative errors away from the calibration point. The model thus captures the correct qualitative trends, with quantitative accuracy strongest near the calibration point and decreasing toward the extremes of the investigated solid-fraction range.

The model captures the increase in stiffness and yield strength with increasing Cu content (higher φ_2). Experimentally, the fracture strain increases significantly with increasing epoxy fraction, whereas epoxy-free HNPCu fractures early within the elastic regime (HNPCu41, Fig. 3b). The abrupt transition toward nearly ideal plastic behavior for the intermediate experimental Epoxy67–HNPCu33 configuration indicates suppression of crack propagation after microcrack initiation. Although the present model does not explicitly predict fracture, it is expected to reproduce the transition from brittle elastic instability in epoxy-free configurations to stable plastic deformation in epoxy-infiltrated composites by resolving stress redistribution and strain localization within the hierarchical network.

Fig. 3b–d further compare selectively infiltrated composites with epoxy-free hierarchical Cu (e.g., HNPCu41), pore-free fully infiltrated reference models (e.g., Full-Epoxy–HNPCu41), and single-scale epoxy–NPCu structures (e.g., Epoxy59–NPCu41). Because the epoxy phase exhibits a very low elastic modulus (E_{epoxy} = 1 MPa), its contribution to the overall elastic stiffness and to the plastic response up to a macroscopic strain of approximately 2% is negligible compared to the Cu network. Consequently, the stress–strain response of epoxy–HNPCu closely matches that of epoxy-free hierarchical nanoporous Cu as well as the pore-free fully infiltrated reference models in the small-strain regime. At larger deformations (>2%), epoxy infiltration leads to slightly higher stresses, as shown in the zoomed-in view in Fig. 3d, attributable to enhanced constraint of plastic deformation and modified stress redistribution within the hierarchical ligament network. The analyzed single-scale epoxy–NPCu structures exhibit significantly higher stiffness and strength compared to their hierarchical counterparts, mainly because the elimination of the lower-level hierarchy effectively increases the effective Cu solid fraction and removes geometrical stress concentration effects. The stiffening mechanisms across configurations are distinct in origin. Between epoxy-free and selectively infiltrated HNPCu, the stress increase beyond 2% strain arises from constraint of ligament rotation, since the epoxy carries negligible stress (Section 4.2). In contrast, the higher stiffness of the non-hierarchical Epoxy59–NPCu41 configuration is purely geometric, resulting from the increased effective load-bearing cross-section when the lower-level ligament network is removed at fixed overall solid fraction φ. This distinction between confinement-driven and geometry-driven stiffening indicates that hierarchy level and infiltration fraction can be tuned independently to target stiffness and ductility separately.

In addition to the axial response, the transverse deformation behavior was evaluated for all three configurations via the apparent Poisson's ratio $\nu_{app} = -\varepsilon_t/\varepsilon_a$, computed from the average transverse displacement of the free lateral unit-cell faces at 2% macroscopic axial strain. Both transverse directions yield closely matching values, confirming the absence of spurious transverse anisotropy. The apparent Poisson's ratio increases monotonically with Cu solid fraction, from $\nu_{app} \approx 0.42$ at $\varphi = 0.10$ and 0.15 to 0.44 at $\varphi = 0.20$, consistently exceeding the elastic Poisson's ratio of bulk Cu ($\nu_{Cu} = 0.34$) due to increasing plastic flow at higher solid fraction. This complements prior scaling analyses of the Poisson's ratio in hierarchical nanoscale networks [25].

Overall, the good agreement between simulations and experiments demonstrates that the hierarchical geometry and calibrated constitutive model capture the essential deformation behavior without explicitly modeling failure.

4.2. Phase-resolved field distributions and deformation localization

To elucidate the micromechanical origin of the macroscopic tensile response, Fig. 4 presents the predicted local equivalent stress distributions at a macroscopic tensile strain of 2%. The macroscopic strain level of 2% is selected as the point at which plastic strain localization becomes statistically resolvable. The elastic-to-yield strain of Cu is very small ($\sigma_0/E_{Cu} \approx 0.015\%$), so plasticity initiates almost immediately at isolated junctions while the network remains largely elastic. By 2% strain, enough ligaments have undergone differential plastic flow that the local stress distribution becomes clearly bimodal (Fig. 4a), reflecting a statistically meaningful localization pattern rather than isolated yielding. This level also remains within the stable hardening region of Epoxy67–HNPCu33 and Epoxy59–HNPCu41 (fracture strains of 17% and 46%), and a single common strain enables controlled comparison across configurations. For the lowest solid fraction (Epoxy78–HNPCu22), 2% exceeds the experimental fracture strain (1.5%), so the corresponding predictions reflect the model's idealized, fracture-free state. The analysis is performed in a phase-resolved manner, separately evaluating the hierarchical Cu phase, the epoxy phase, epoxy-free HNPCu, and pore-free fully infiltrated reference structures. This approach enables direct assessment of possible load transfer and stress redistribution across the different hierarchical configurations. To better resolve the critical high-stress tail of the distributions, a semi-logarithmic representation is employed. Fig. 4a shows the local stress distributions within the Cu phase of the three selectively infiltrated composites. All configurations exhibit a pronounced bimodal distribution with maximum equivalent stresses reaching approximately 80 MPa. The local equivalent stress distributions exhibit a bimodal character, with a pronounced peak at the initial yield stress of 20 MPa separating elastically loaded regions from plastically deforming ligaments undergoing strain hardening. With increasing Cu solid fraction, the probability of high local stresses increases slightly, resulting in a more heterogeneous stress field. Stress concentrations are predominantly localized within the Cu ligament network, whereas the epoxy phase carries significantly lower stresses due to its low stiffness, with maximum values below <0.5 MPa (Fig. 4b). For the Epoxy59–HNPCu41 configuration, the average local equivalent stress in the Cu phase is approximately 27 ± 15 MPa, whereas the epoxy phase carries only about 0.04 ± 0.02 MPa, corresponding to a stress contrast ratio of roughly 675. A similarly pronounced partitioning is observed for Epoxy78–HNPCu22, with average local stresses of 23 ± 14 MPa in Cu and 0.03 ± 0.02 MPa in epoxy, indicating that the metallic network remains the dominant load-bearing phase irrespective of epoxy fraction.

The stress contrast exceeding 600 across all solid fractions reflects the large elastic mismatch between the phases ($E_{Cu}/E_{epoxy} \approx 1.3 \times 10^5$), well beyond typical fiber- or particle-reinforced composites. In this regime, the epoxy acts as a kinematic constraint rather than a co-loaded reinforcing phase. The sensitivity of this conclusion to the assumed epoxy modulus was verified by an additional simulation for Epoxy78–HNPCu22 using a strongly reduced, near-void modulus of $E_{epoxy} = 0.01$ MPa. This reduction measurably lowers the macroscopic stress (by approximately 6.6% at 5% strain), indicating that the epoxy's finite stiffness, despite carrying negligible stress itself, measurably stabilizes the deformation process rather than merely bearing load. The mechanically decisive property may be less E_{epoxy} itself than the epoxy's

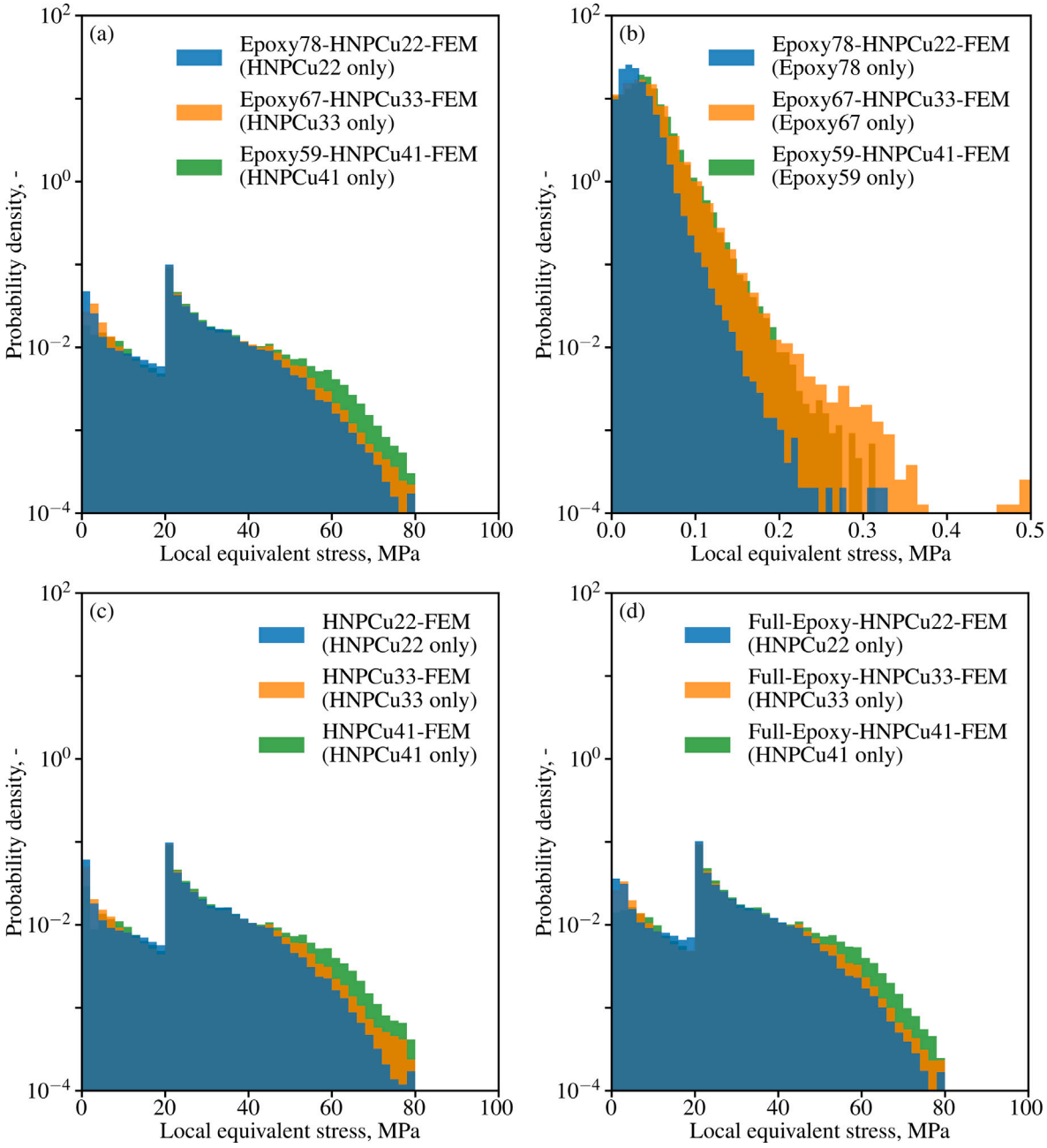

Fig. 4. FE prediction of local equivalent stress distributions at 2% macroscopic tensile strain. **(a)** Hierarchical Cu phase only in the epoxy–HNPCu composite for Epoxy78–HNPCu22, Epoxy67–HNPCu33, and Epoxy59–HNPCu41. **(b)** Corresponding epoxy phase only for the three composite models, and **(c)** epoxy-free HNPCu configurations. **(d)** Hierarchical Cu phase only in pore-free full-epoxy structures.

near-incompressibility (ν_{epoxy} = 0.49): filled pores cannot be volumetrically compacted force-free, constraining the Cu network independent of exact stiffness, also explaining why rate-dependence would not alter this conclusion, since the relevant state is the equilibrium (relaxed) configuration rather than the transient response. Rate-dependence is not specific to the epoxy phase: nanoporous metals themselves exhibit rate-dependent (creep) behavior, as reported experimentally by several groups [82], making this a broader open question for the field. It remains unresolved even for single-hierarchy-level nanoporous metals with current methods, given the geometric complexity involved, not a limitation specific to the present system. The consistently high stress contrast (>600) across all configurations confirms that the primary mechanical role of the flexible epoxy is structural stabilization rather than load transfer. Similar local equivalent stress distributions in the Cu phase are predicted for the epoxy-free hierarchical configurations (Fig. 4c) and the pore-free fully infiltrated structures (Fig. 4d).

To further elucidate the deformation mechanisms governing the macroscopic tensile response, Fig. 5 presents the predicted local equivalent plastic strain in the Cu phase and maximum principal strain distributions at a macroscopic tensile strain of 2%. The phase-resolved analysis enables direct comparison of strain localization in selectively infiltrated composites, epoxy-free hierarchical HNPCu, and pore-free fully infiltrated reference structures. Fig. 5a shows the equivalent plastic strain distribution within the hierarchical Cu phase of the selectively infiltrated composites. A clear reduction in plastic strain localization is observed with increasing Cu solid fraction. For the Epoxy59–HNPCu41 configuration, the maximum plastic strain reaches values slightly below 20%, as indicated by the arrow. In contrast, lower solid fraction configurations exhibit more pronounced strain concentrations, with peak

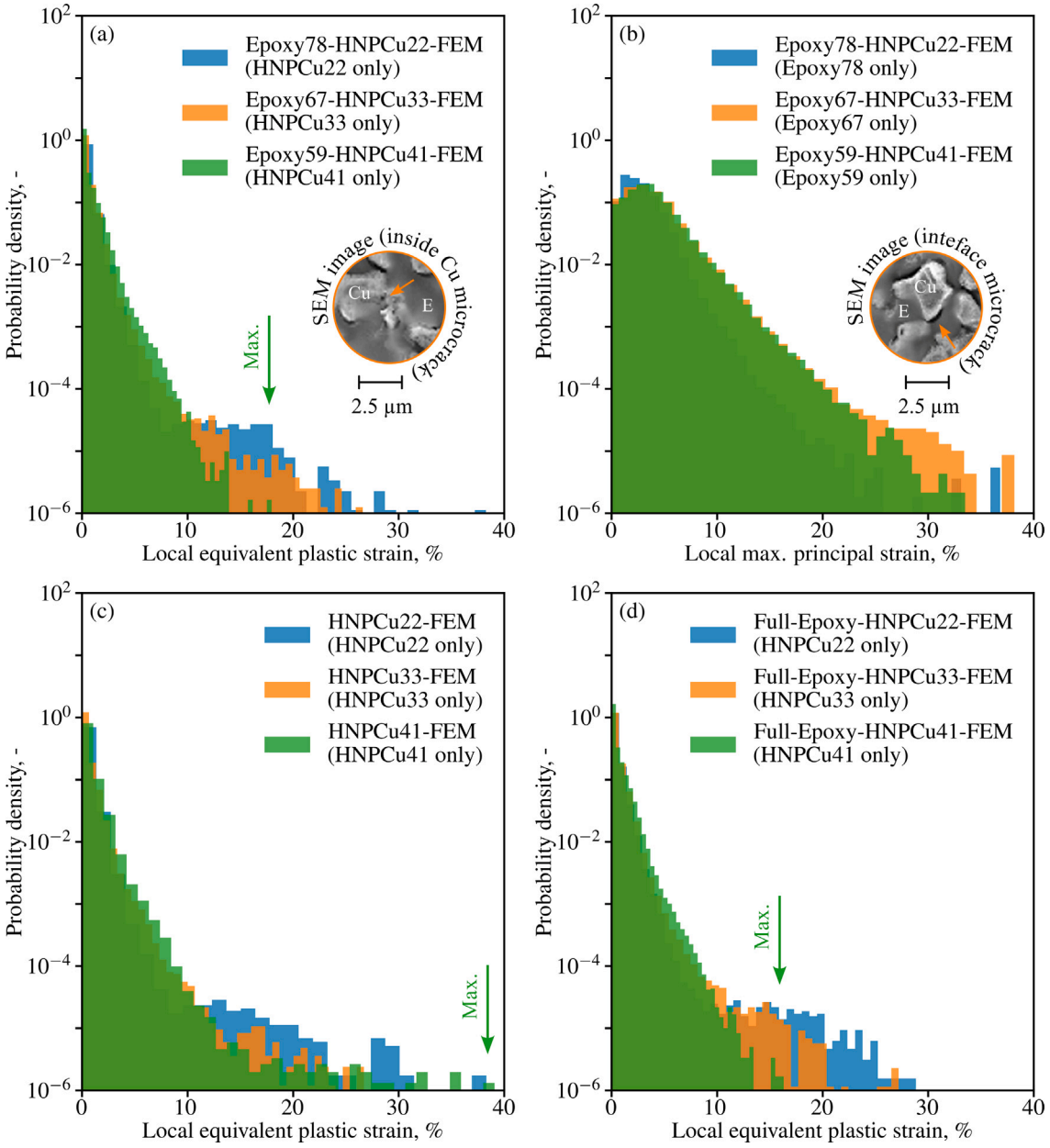

Fig. 5. FE prediction of local equivalent plastic strain **(a, c, d)** and maximum principal strain **(d)** distributions at 2% macroscopic tensile strain. **(a)** Hierarchical Cu phase only in the epoxy–HNPCu composite for Epoxy78–HNPCu22, Epoxy67–HNPCu33, and Epoxy59–HNPCu41. **(b)** Corresponding epoxy phase only for the three composite models, and **(c)** epoxy-free HNPCu configurations. **(d)** Hierarchical Cu phase only in pore-free full-epoxy structures. Arrows indicate the maximum plastic strain found in the different HNPCu41 configurations. Representative SEM images of Epoxy67–HNPCu33 included in (a) and (b) reveal microcracks within the Cu ligament network and at the Cu–epoxy interface, respectively, adapted from [28] with permission from Elsevier.

values approaching 40%. The denser upper-level ligament network provides enhanced load redistribution pathways, thereby reducing strain amplification at individual junctions. Since the epoxy phase is modeled as purely elastic, equivalent plastic strain is not defined in Fig. 5b. Instead, the maximum principal strain is evaluated to characterize tensile deformation within the polymer phase. This measure is particularly relevant because tensile principal strains are associated with potential crack initiation in brittle or weakly ductile polymers [83]. The maximum principal strain distributions in the epoxy phase appear qualitatively similar across all configurations. For Epoxy59–HNPCu41, the average principal strain within the epoxy phase is approximately 3.6 ± 2.4%, whereas the corresponding average strain within the Cu phase is about 0.46 ± 0.72%. For Epoxy78–HNPCu22, the average values are 2.6 ± 1.6% in epoxy and 0.32 ± 0.56% in Cu, respectively. This pronounced strain contrast highlights the strong deformation partitioning between the compliant polymer and the metallic ligament network. The strain contrast between epoxy and Cu remains on the order of 8 across configurations, indicating robust phase-wise deformation partitioning.

Together, the strain contrast of approximately 8 and the stress contrast exceeding 600 quantify the double-network character of the composite: the Cu network carries the load at comparatively small strains, while the epoxy accommodates large local strains at negligible stress. This partitioning underlies the progressive reduction in peak plastic strain with increasing confinement (from ~40% in epoxy-free HNPCu to below 20% in selectively infiltrated composites and below 15% in fully infiltrated structures) providing a quantitative, hierarchy-resolved analogue to toughening in natural hard–soft composites such

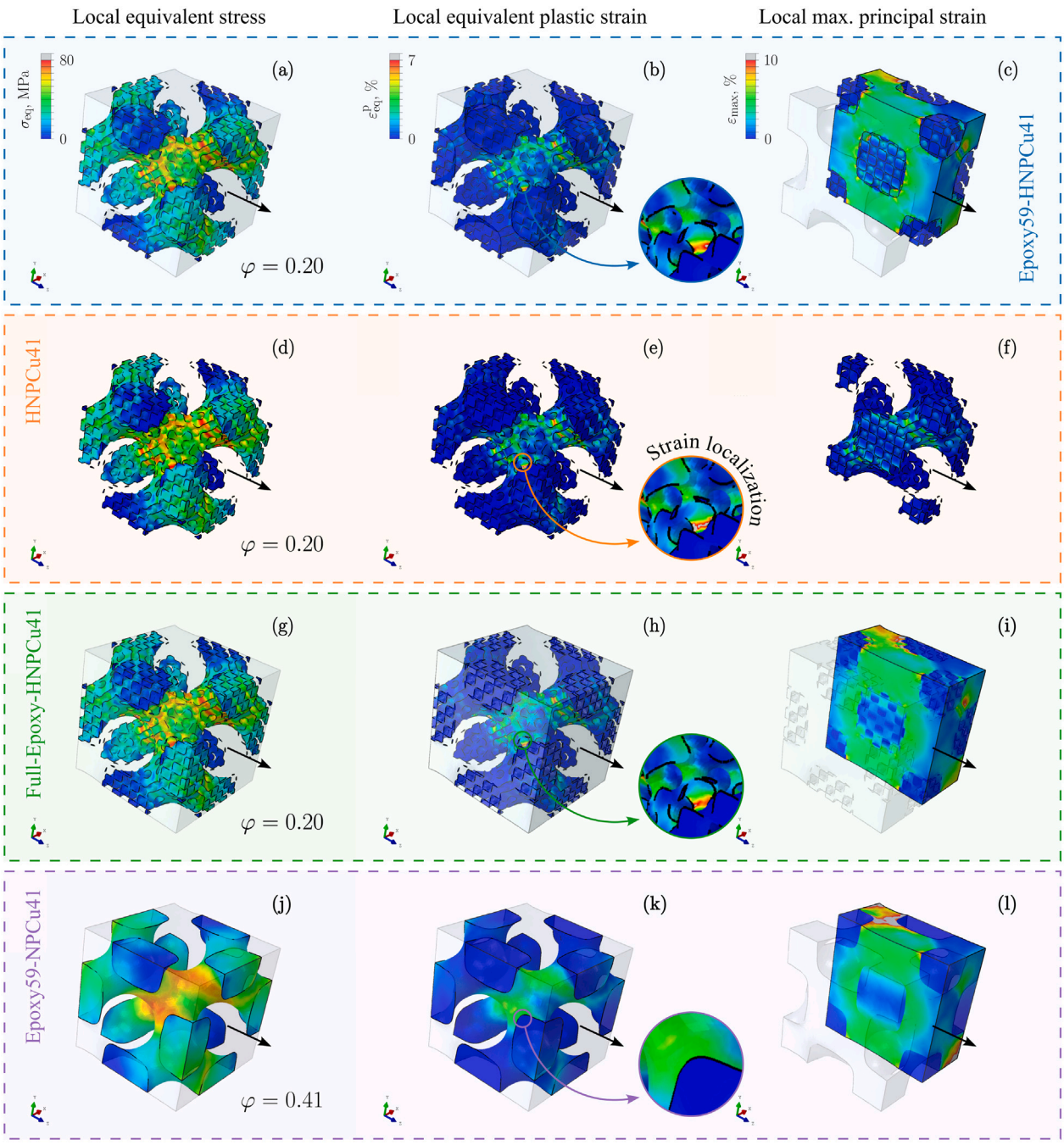

Fig. 6. Predicted contour plots at 2% macroscopic tensile strain for local equivalent stress σ_{eq} **(a, d, g, j)**, equivalent plastic strain ε^p_{eq} **(b, e, h, k)**, and maximum principal strain ε_{max} **(c, f, i, l)**. **(a–c)** Epoxy59–HNPCu41, including a zoomed-in view highlighting pronounced plastic strain localization within the hierarchical Cu phase. **(d–f)** Epoxy-free HNPCu41, **(g–i)** pore-free full-epoxy HNPCu41, and **(j–l)** non-hierarchical single-scale Epoxy59–NPCu41.

as bone and nacre. Most notably, in the absence of epoxy (Fig. 5c), plastic strain localization becomes significantly more pronounced for all configurations. For the HNPCu41 structure, the maximum plastic strain approaches 40%, nearly twice the value observed in the selectively infiltrated counterpart (Fig. 5a). The absence of polymer constraint promotes intense strain amplification at ligament junctions, indicating reduced deformation stability. Complete polymer embedding (Fig. 5d) even further suppresses plastic strain localization for all configurations. For Epoxy59–HNPCu41, the maximum plastic strain decreases to values around 15%, indicating that the surrounding polymer laterally constrains ligament deformation, suppressing the necking-type localization that drives strain amplification at junctions in the unconstrained case.

The results demonstrate that the primary mechanical function of the flexible epoxy is not load bearing, but deformation stabilization. Although the epoxy phase carries negligible stress, it suppresses lateral expansion at ligament junctions, redistributing tensile strains and thereby preventing extreme plastic strain localization. At identical macroscopic strain, the maximum local plastic strain decreases from approximately 40% in epoxy-free HNPCu to below 20% in selectively infiltrated composites and further to below 15% in fully infiltrated structures, clearly demonstrating the progressive attenuation of strain amplification due to polymer confinement. This marked reduction in localization intensity provides a micromechanical explanation for the experimentally observed transition from brittle elastic fracture to more stable plastic deformation.

To further clarify the spatial characteristics of deformation localization, Fig. 6 presents corresponding contour plots of equivalent stress σ_{eq}, equivalent plastic strain ε^{p}_{eq}, and maximum principal strain ε_{max} at a macroscopic tensile strain of 2%. The comparison focuses on the Epoxy59–HNPCu41 configuration and its corresponding epoxy-free, fully infiltrated, and non-hierarchical single-scale counterparts, enabling again direct assessment of the role of polymer confinement and hierarchical architecture.

For the selectively infiltrated Epoxy59–HNPCu41 composite (Fig. 6a–c), stress and plastic strain concentrations are primarily located at ligament junctions and highly curved segments of the hierarchical Cu network. The zoomed-in view highlights pronounced plastic strain accumulation on the outer faces of the Cu ligaments, particularly at junction regions. The maximum principal strain field reveals pronounced strain localization at the Cu–epoxy interfaces, where significantly higher tensile strain values develop in the epoxy phase compared to the surrounding Cu ligaments. These interface regions therefore represent another preferred sites for microcrack initiation, consistent with the experimentally observed crack formation along phase boundaries [28,51] (Fig. 5b).

In the epoxy-free HNPCu41 structure (Fig. 6d–f), the spatial locations of strain hot spots remain largely unchanged. However, the intensity of plastic strain localization is slightly amplified. Ligament junctions experience higher strain accumulation, consistent with the previously observed increase in maximum plastic strain to nearly 40%. In the absence of polymer constraint, ligaments are free to bend and rotate more, resulting in amplified local strains. The pore-free fully infiltrated structure (Fig. 6g–i) exhibits similar stress and strain fields as in Fig. 6a–c. Complete polymer embedding restricts ligament bending and reduces rotational degrees of freedom at junctions, thereby attenuating strain concentrations and stabilizing the deformation pattern. The non-hierarchical single-scale Epoxy59–NPCu41 configuration (Fig. 6j–l) displays a distinctly different deformation pattern. In the absence of the lower hierarchical level, strain localization is less influenced by multiscale junction interactions, and the deformation appears more uniformly distributed along the ligaments. In analogy to weak-link theory, subdividing coarse ligaments into finer hierarchical networks multiplies the number of junction sites available for strain localization, governing the overall deformation pathway and localization intensity.

Overall, the contour analysis confirms that epoxy infiltration does not fundamentally alter the spatial deformation mode of the hierarchical Cu network, but rather suppresses the intensity of strain amplification at critical ligament junctions. The preservation of localization sites combined with reduced peak strain levels supports the interpretation that polymer confinement stabilizes the network against catastrophic local failure without significantly modifying the global load-bearing mechanism.

The predicted localization patterns agree well with the in-situ SEM observations of epoxy–HNPCu composites [28]. Experimentally, microcracks form predominantly at Cu–epoxy interfaces and occasionally within the nanoporous Cu phase [28,51] (Fig. 5a, b). The simulations reproduce this behavior. In epoxy-free configurations, plastic strain amplification is most pronounced, promoting rapid instability, whereas epoxy confinement reduces peak strain levels while preserving the overall deformation mode. This suppression of strain localization stabilizes the hierarchical Cu network and delays crack initiation and coalescence. These findings support the experimentally proposed double-network toughening mechanism, where the stiff Cu network bears the load and the compliant epoxy phase constrains deformation and mitigates damage evolution. This toughening strategy shares its underlying principle (a stiff, load-bearing phase combined with a compliant phase that constrains deformation) with natural hierarchical hard–soft composites such as nacre and bone. In nacre, staggered mineral platelets separated by thin organic layers promote crack deflection and cooperative plastic deformation of platelet stacks [84]. In bone, a mineralized collagen matrix similarly dissipates energy through hierarchy-spanning mechanisms [85]. The present system differs mechanistically, as the epoxy remains perfectly bonded and suppresses ligament rotation through continuum confinement rather than interfacial sliding, yet the macroscopic outcome (a passive soft phase delaying catastrophic failure) is analogous. Similar confinement-driven toughening has recently been demonstrated in bio-inspired cementitious composites [86] and in auxetic cementitious composites where stiffness contrast between phases governs confinement [87], supporting the generality of the mechanism identified here.

The identified toughening mechanism does not map onto classical homogenization schemes such as Mori–Tanaka or self-consistent methods, which target effective moduli under smoothly distributed reinforcement rather than localized strain concentration at discrete network junctions. It is instead consistent with a weak-link, junction-controlled picture, where polymer confinement suppresses the intensity, rather than the spatial distribution, of strain concentration (Section 4.2). As a first-order description, a confinement factor $g(c) = \varepsilon^{p}_{max}/\varepsilon^{p}_{max,0}$ at fixed solid fraction ($\varphi = 0.20$, $\varepsilon^{p}_{max,0} \approx 40\%$) yields $g \approx 1$, 0.5, and 0.375 for epoxy-free, selectively infiltrated, and fully infiltrated structures. A comparable reduction occurs with increasing solid fraction at fixed confinement, indicating that hierarchy and infiltration both independently promote stabilization. However, the dataset does not sample enough combinations to establish how these effects combine, leaving a fully decoupled scaling relation for future, systematic parametric work.

5. Conclusions

This study provides micromechanical insight into the tensile deformation of epoxy-filled hierarchical nanoporous Cu, using an experimentally informed FE framework with explicitly resolved hierarchical architecture. Despite the geometric idealization of the ligament network, the calibrated model reproduces the experimentally observed tensile trends across the investigated solid-fraction range, capturing the transition from brittle, elastic-dominated behavior in epoxy-free HNPCu to stable plastic deformation in epoxy-infiltrated composites. Agreement with experiment is close for the calibrated configuration and differs more markedly for the non-calibrated ones, indicating that hierarchy-governed mechanisms are captured qualitatively, with quantitative accuracy strongest near the calibration point.

Phase-resolved analysis shows that epoxy infiltration leaves the macroscopic tensile response largely unaffected at small strains, since the compliant polymer carries negligible stress relative to the Cu network (stress contrast >600). At larger strains, however, infiltration markedly reduces plastic strain localization within the Cu network (lowering the peak local plastic strain from approximately 40% in epoxy-free HNPCu to below 15% in fully infiltrated structures) by constraining ligament rotation at junctions rather than by direct load bearing. This confinement-driven stabilization, rather than reinforcement, is the primary mechanical function of the polymer phase, analogous to double-network toughening in biological hard–soft composites.

Strain localization develops both at Cu–epoxy interfaces and within the Cu ligament network itself. While interfacial regions are established microcrack-initiation sites, localization inside the Cu network (consistent with experimentally observed microcracks within the ligaments) identifies the hierarchical architecture itself as an additional, previously underappreciated source of failure susceptibility. Together, these findings establish a micromechanical basis for microstructure-guided design of hierarchical nanoporous metal–polymer composites, where hierarchy level and infiltration fraction can be tuned independently to target stiffness, ductility, and damage tolerance.

While applied here to epoxy-infiltrated hierarchical nanoporous Cu, the modeling approach (explicit resolution of hierarchical ligament networks with selective infiltration) is not specific to this system. It is directly transferable to other dealloyed hierarchical nanoporous metals (e.g., Au, Ag, Ni) and alternative polymers, given the corresponding structural and constitutive parameters, and the confinement-based toughening mechanism is expected to generalize whenever a compliant phase constrains a stiffer hierarchical network.

CRediT authorship contribution statement

Tim Fischer: Writing – original draft, Visualization, Validation, Software, Methodology, Investigation, Formal analysis, Conceptualization. **Norbert Huber:** Writing – review & editing, Supervision, Resources, Project administration, Funding acquisition.

Declaration of competing interest

The authors declare that they have no known competing financial interests or personal relationships that could have appeared to influence the work reported in this paper.

Acknowledgments

This work was supported by the Deutsche Forschungsgemeinschaft (DFG, German Research Foundation) through the Cluster of Excellence EXC3120 BlueMat: Water-Driven Materials (533771286) and the Hamburg Centre for Integrated Multiscale Materials Systems (CIMMS). The authors gratefully acknowledge the TUHH Computing Center for access to the high-performance computing (HPC) cluster. Special thanks are extended to S. Dangol (Hamburg University of Technology) for support with hierarchical model generation.

Data availability

Data will be made available on request.

References

[1] Erlebacher J, Aziz MJ, Karma A, Dimitrov N, Sieradzki K. Evolution of nanoporosity in dealloying. Nature 2001;410(6827):450–3. http://dx.doi.org/10.1038/35068529.

[2] Weissmüller J, Newman RC, Jin H-J, Hodge AM, Kysar JW. Nanoporous metals by alloy corrosion: Formation and mechanical properties. MRS Bull 2009;34(8):577–86. http://dx.doi.org/10.1557/mrs2009.157.

[3] Ding Y, Kim Y-J, Erlebacher J. Nanoporous gold leaf: "ancient technology"/advanced material. Adv Mater 2004;16(21):1897–900. http://dx.doi.org/10.1002/adma.200400792.

[4] Wittstock A, Zielasek V, Biener J, Friend CM, Bäumer M. Nanoporous gold catalysts for selective gas-phase oxidative coupling of methanol at low temperature. Science 2010;327(5963):319–22. http://dx.doi.org/10.1126/science.1183591.

[5] Chen L-Y, Yu J-S, Fujita T, Chen M-W. Nanoporous copper with tunable nanoporosity for SERS applications. Adv Funct Mater 2009;19(8):1221–6. http://dx.doi.org/10.1002/adfm.200801239.

[6] Weissmüller J, Viswanath RN, Kramer D, Zimmer P, Würschum R, Gleiter H. Charge-induced reversible strain in a metal. Science 2003;300(5617):312–5. http://dx.doi.org/10.1126/science.1081024.

[7] Biener J, Wittstock A, Zepeda-Ruiz L, Biener M, Zielasek V, Kramer D, Viswanath R, Weissmüller J, Bäumer M, Hamza A. Surface-chemistry-driven actuation in nanoporous gold. Nat Mater 2009;8:47–51. http://dx.doi.org/10.1038/nmat2335.

[8] Jin H-J, Weissmüller J. A material with electrically tunable strength and flow stress. Science 2011;332(6034):1179–82. http://dx.doi.org/10.1126/science.1202190.

[9] Jin H-J, Weissmüller J. Bulk nanoporous metal for actuation. Adv Eng Mater 2010;12(8):714–23. http://dx.doi.org/10.1002/adem.200900329.

[10] Tan F, Yu B, Yan X, Zhang Y, Bai Q, Zhang J, Zhang Z. Electrochemical actuation behaviors of bulk nanoporous copper with a hierarchical structure. J Alloys Compd 2022;923:166469. http://dx.doi.org/10.1016/j.jallcom.2022.166469.

[11] Lang X, Hirata A, Fujita T, Chen M. Nanoporous metal/oxide hybrid electrodes for electrochemical supercapacitors. Nat Nanotechnol 2011;6(4):232–6. http://dx.doi.org/10.1038/nnano.2011.13.

[12] Zhao H, Lei D, He Y-B, Yuan Y, Yun Q, Ni B, Lv W, Li B, Yang Q-H, Kang F, Lu J. Compact 3D copper with uniform porous structure derived by electrochemical dealloying as dendrite-free lithium metal anode current collector. Adv Energy Mater 2018;8(19):1800266. http://dx.doi.org/10.1002/aenm.201800266.

[13] Meng H, Ran Q, Dai T-Y, Jia J-H, Liu J, Shi H, Han G-F, Wang T-H, Wen Z, Lang X-Y, Jiang Q. Lamellar nanoporous metal/intermetallic compound heterostructure regulating dendrite-free zinc electrodeposition for wide-temperature aqueous zinc-ion battery. Adv Mater 2024;36(26):2403803. http://dx.doi.org/10.1002/adma.202403803.

[14] Chen Q, Ding Y, Chen M. Nanoporous metal by dealloying for electrochemical energy conversion and storage. MRS Bull 2018;43(1):43–8. http://dx.doi.org/10.1557/mrs.2017.300.

[15] Gleiter H, Weissmüller J, Wollersheim O, Würschum R. Nanocrystalline materials: a way to solids with tunable electronic structures and properties? Acta Mater 2001;49(4):737–45. http://dx.doi.org/10.1016/S1359-6454(00)00221-4.

[16] Wang L, Xie H, Shao J-C, Yang H, Feng P-Z, Jin H-J. High-strength hierarchical-structured bulk nanoporous Cu prepared by dealloying and spark plasma sintering. Scr Mater 2021;203:114114. http://dx.doi.org/10.1016/j.scriptamat.2021.114114.

[17] Sun S, Wang W, Zhang C, Liu W, Godfrey A. Synthesis and mechanical properties of low crack-density bulk hierarchical nanoporous copper. Scr Mater 2025;258:116531. http://dx.doi.org/10.1016/j.scriptamat.2024.116531.

[18] Zhong H, Song T, Liu H, Li C, Li C, Wen M, Ning Z, Gu J, Qian M. Skeletal high-strength nanoporous copper and metamaterials: The Hakka Tulou design heritage. Adv Mater 2025;37(47):e03701. http://dx.doi.org/10.1002/adma.202503701.

[19] Gwak E-J, Jeon H, Song E, Kang N-R, Kim J-Y. Twinned nanoporous gold with enhanced tensile strength. Acta Mater 2018;155:253–61. http://dx.doi.org/10.1016/j.actamat.2018.06.009.

[20] Kashani H, Chen M. Flaw-free nanoporous Ni for tensile properties. Acta Mater 2019;166:402–12. http://dx.doi.org/10.1016/j.actamat.2018.12.056.

[21] Shi S, Li Y, Ngo-Dinh B-N, Markmann J, Weissmüller J. Scaling behavior of stiffness and strength of hierarchical network nanomaterials. Science 2021;371(6533):1026–33. http://dx.doi.org/10.1126/science.abd9391.

[22] Biener J, Hodge AM, Hayes JR, Volkert CA, Zepeda-Ruiz LA, Hamza AV, Abraham FF. Size effects on the mechanical behavior of nanoporous Au. Nano Lett 2006;6(10):2379–82. http://dx.doi.org/10.1021/nl061978i.

[23] Peng Wu L-ZL, Jin H-J. Monolayer oxide enhanced flow stress in nanoporous gold: the size dependence. Mater Res Lett 2018;6(9):508–14. http://dx.doi.org/10.1080/21663831.2018.1486337.

[24] Engelman B, Mathesan S, Fedyaeva T, Bisht A, Rabkin E, Mordehai D. Deformation behavior of nanoporous gold nanoparticles during compression. Acta Mater 2025;286:120723. http://dx.doi.org/10.1016/j.actamat.2025.120723.

[25] Sun H, Lührs L, Chang W-C, Shi S. Scaling behavior of Poisson's ratio in hierarchical nanoscale network materials. Acta Mater 2025;298:121393. http://dx.doi.org/10.1016/j.actamat.2025.121393.

[26] Wang K, Weissmüller J. Composites of nanoporous gold and polymer. Adv Mater 2013;25(9):1280–4. http://dx.doi.org/10.1002/adma.201203740.

[27] Wang K, Kobler A, Kübel C, Jelitto H, Schneider G, Weissmüller J. Nanoporous-gold-based composites: toward tensile ductility. NPG Asia Mater 2015;7(6):e187. http://dx.doi.org/10.1038/am.2015.58.

[28] Wang L, Xie H, Jin H-J. Epoxy-infiltrated hierarchical nanoporous Cu with exceptional ductility and surface-enabled functions. J Mater Sci Technol 2025;238:78–85. http://dx.doi.org/10.1016/j.jmst.2025.01.084.

[29] Jeon H, Lee S, Kim J-Y. Tension-compression asymmetry in plasticity of nanoporous gold. Acta Mater 2020;199:340–51. http://dx.doi.org/10.1016/j.actamat.2020.08.054.

[30] Li R, Sieradzki K. Ductile-brittle transition in random porous au. Phys Rev Lett 1992;68:1168–71. http://dx.doi.org/10.1103/PhysRevLett.68.1168.

[31] Biener J, Hodge AM, Hamza AV. Microscopic failure behavior of nanoporous gold. Appl Phys Lett 2005;87(12):121908. http://dx.doi.org/10.1063/1.2051791.

[32] Jin H-J, Kurmanaeva L, Schmauch J, Rösner H, Ivanisenko Y, Weissmüller J. Deforming nanoporous metal: Role of lattice coherency. Acta Mater 2009;57(9):2665–72. http://dx.doi.org/10.1016/j.actamat.2009.02.017.

[33] Balk TJ, Eberl C, Sun Y, Hemker KJ, Gianola DS. Tensile and compressive microspecimen testing of bulk nanoporous gold. JOM 2009;61(12):26–31. http://dx.doi.org/10.1007/s11837-009-0176-6.

[34] Briot NJ, Kennerknecht T, Eberl C, Balk TJ. Mechanical properties of bulk single crystalline nanoporous gold investigated by millimetre-scale tension and compression testing. Phil Mag 2014;94(8):847–66. http://dx.doi.org/10.1080/14786435.2013.868944.

[35] Badwe N, Chen X, Sieradzki K. Mechanical properties of nanoporous gold in tension. Acta Mater 2017;129:251–8. http://dx.doi.org/10.1016/j.actamat.2017.02.040.

[36] Lee D, Wei X, Chen X, Zhao M, Jun S, Hone J, Herbert EG, Oliver WC, Kysar JW. Microfabrication and mechanical properties of nanoporous gold at the nanoscale. Scr Mater 2007;56(5):437–40. http://dx.doi.org/10.1016/j.scriptamat.2006.08.069.

[37] Lee D, Wei X, Zhao M, Chen X, Jun SC, Hone J, Kysar JW. Plastic deformation in nanoscale gold single crystals and open-celled nanoporous gold. Model Simul Mater Sci Eng 2006;15(1):S181. http://dx.doi.org/10.1088/0965-0393/15/1/S15.

[38] Yang W, Luo Z-P, Bao W-K, Xie H, You Z-S, Jin H-J. Light, strong, and stable nanoporous aluminum with native oxide shell. Sci Adv 2021;7(28):eabb9471. http://dx.doi.org/10.1126/sciadv.abb9471.

[39] Lu Z-J, Liu L-Z, Xie H, Jin H-J. Capillary shrinkage induced ductile–brittle transition in nanoporous gold: Crack healing via cold welding. Acta Mater 2025;292:120997. http://dx.doi.org/10.1016/j.actamat.2025.120997.

[40] Xie H, Shao J-C, Zou L, Jin H-J. Weak boundary enabled tensile ductility in dealloyed porous fe alloy. Acta Mater 2023;243:118501. http://dx.doi.org/10.1016/j.actamat.2022.118501.
[41] Ji Y, Xing Y, Zhou F, Li X, Chen Y, Shao L-H. The mechanical characteristics of monolithic nanoporous copper and its composites. Adv Eng Mater 2018;20(10):1800574. http://dx.doi.org/10.1002/adem.201800574.
[42] Chen J-J, Xie H, Liu L-Z, Guan H, You Z, Zou L, Jin H-J. Strengthening gold with dispersed nanovoids. Science 2024;385(6709):629–33. http://dx.doi.org/10.1126/science.abo7579.
[43] Hablitzel MP, Lilleodden ET. On measuring the independent mechanical response of the polymer phase from nanoporous gold polymer composites. Scr Mater 2019;170:67–70. http://dx.doi.org/10.1016/j.scriptamat.2019.04.026.
[44] Wang E, Yao R, Li Q, Hu X, Sun G. Lightweight metallic cellular materials: A systematic review on mechanical characteristics and engineering applications. Int J Mech Sci 2024;270:108795. http://dx.doi.org/10.1016/j.ijmecsci.2023.108795.
[45] Yuan J, Wang Z, Shang Y, Hua J, Lu L, Cai Y, Luo S. Compression behavior of a resin/alumina interpenetrating phase composite. Int J Mech Sci 2025;297–298:110347. http://dx.doi.org/10.1016/j.ijmecsci.2025.110347.
[46] Mu Y, Jin Y, Ji H, Luo J, Li G, Xu M, Li H, Deng B, Du J. Mechanical performance of interpenetrating phase composites with multi-sheet lattice structures. Int J Mech Sci 2024;276:109369. http://dx.doi.org/10.1016/j.ijmecsci.2024.109369.
[47] Albertini F, Dirrenberger J, Sollogoub C, Molotnikov A, Adrien J, Maire E. Hybrid auxetics: Postponing failure with elastomer infiltration of Ti-6Al-4V lattices. Int J Mech Sci 2025;306:110704. http://dx.doi.org/10.1016/j.ijmecsci.2025.110704.
[48] Anandan N, Wilson CG, Meza LR. Functionally graded spinodal nanoarchitected ceramics with unprecedented recoverability. Int J Mech Sci 2025;301:110453. http://dx.doi.org/10.1016/j.ijmecsci.2025.110453.
[49] Ngô B-ND, Stukowski A, Mameka N, Markmann J, Albe K, Weissmüller J. Anomalous compliance and early yielding of nanoporous gold. Acta Mater 2015;93:144–55. http://dx.doi.org/10.1016/j.actamat.2015.04.021.
[50] Griffiths E, Wilmers J, Bargmann S, Reddy BD. Nanoporous metal based composites: Giving polymers strength and making metals move. J Mech Phys Solids 2020;137:103848. http://dx.doi.org/10.1016/j.jmps.2019.103848.
[51] Griffiths E, Soyarslan C, Bargmann S, Reddy B. Insights into fracture mechanisms in nanoporous gold and polymer impregnated nanoporous gold. Extrem Mech Lett 2020;39:100815. http://dx.doi.org/10.1016/j.eml.2020.100815.
[52] Bargmann S, Soyarslan C, Husser E, Konchakova N. Materials based design of structures: Computational modeling of the mechanical behavior of gold-polymer nanocomposites. Mech Mater 2016;94:53–65. http://dx.doi.org/10.1016/j.mechmat.2015.11.008.
[53] Li J, Tian C, Lu B, Xian Y, Wu R, Hu G, Xia R. Deformation behavior of nanoporous gold based composite in compression: A finite element analysis. Compos Struct 2019;211:229–35. http://dx.doi.org/10.1016/j.compstruct.2018.12.046.
[54] Gnegel S, Li J, Mameka N, Huber N, Düster A. Numerical investigation of polymer coated nanoporous gold. Materials 2019;12(13). http://dx.doi.org/10.3390/ma12132178.
[55] Dyckhoff L, Huber N. Data-driven modelling of the multiaxial yield behaviour of nanoporous metals. Int J Mech Sci 2023;259:108601. http://dx.doi.org/10.1016/j.ijmecsci.2023.108601.
[56] Dyckhoff L, Huber N. Physics-informed recurrent neural networks for predicting elasto-plastic behavior in hierarchical finite element modeling. Proc Appl Math Mech 2026;26:e70148. http://dx.doi.org/10.1002/pamm.70148.
[57] Li Y, Hu K, Lilleodden ET, Huber N. Datasets for structural and mechanical properties of nanoporous networks from FIB reconstruction. Data Brief 2025;63:112152. http://dx.doi.org/10.1016/j.dib.2025.112152.
[58] Przybilla T, Xie Z, Prakash A, Thiess E, Niekiel F, Zubiri BA, Mačković M, Schweizer P, Guénolé J, Kelly ST, Bale HA, Wang D, Sandfeld S, Bitzek E, Spiecker E. Revealing nanoscale plasticity of metallic nanosponges with correlative and scale-bridging 3D microscopy and modelling. Commun Mater 2025;6(1):204. http://dx.doi.org/10.1038/s43246-025-00914-z.
[59] Rodriguez S, Calius E, Khatibi A, Orifici A, Das R. Hierarchical design of mechanical metamaterials: an application on pentamode-like structures. Int J Mech Sci 2025;294:110232. http://dx.doi.org/10.1016/j.ijmecsci.2025.110232.
[60] Wu J, Yang F, Li L, Li P, Xu X, Zhang Y. Multi-feature bionic gradient hierarchical lattice metamaterials with multi-synergistic crushing mechanisms. Int J Mech Sci 2024;283:109383. http://dx.doi.org/10.1016/j.ijmecsci.2024.109383.
[61] Hu Z, Ding J, Ma WWS, Li R, Mo H, Song X. Mechanically efficient hierarchical lattices via plate-tpms architecture. Int J Mech Sci 2026;316:111449. http://dx.doi.org/10.1016/j.ijmecsci.2026.111449.
[62] Jeon H, Markmann J, Shi S. Effects of structural hierarchy and size on mechanical behavior of nanoporous gold. Acta Mater 2024;273:119954. http://dx.doi.org/10.1016/j.actamat.2024.119954.
[63] Ying J, Lenaerts S, Symes MD, Yang X-Y. Hierarchical design in nanoporous metals. Adv Sci 2022;9(27):2106117. http://dx.doi.org/10.1002/advs.202106117.
[64] Huber N, Viswanath R, Mameka N, Markmann J, Weißmüller J. Scaling laws of nanoporous metals under uniaxial compression. Acta Mater 2014;67:252–65. http://dx.doi.org/10.1016/j.actamat.2013.12.003.
[65] Fischer T, Huber N. Designing microcompression experiments for nanoporous metals via computational plasticity. Mater Des 2025;258:114550. http://dx.doi.org/10.1016/j.matdes.2025.114550.
[66] Fischer T, Huber N. Microstructure and orientation effects on microcompression-induced plasticity in nanoporous gold. Acta Mater 2026;304:121798. http://dx.doi.org/10.1016/j.actamat.2025.121798.
[67] Jiao J, Huber N. Effect of nodal mass on macroscopic mechanical properties of nanoporous metals. Int J Mech Sci 2017;134:234–43. http://dx.doi.org/10.1016/j.ijmecsci.2017.10.011.
[68] Ma S, Dai Y, Liu Y. Investigation of creep behaviors in three-dimensional porous sintered silver by FFT homogenization. Int J Mech Sci 2025;297–298:110275. http://dx.doi.org/10.1016/j.ijmecsci.2025.110275.
[69] Gómez IG, Lorca YE, Velilla-Díaz W, Pacheco-Sanjuán A. Elastic constants and material stability analysis of orthotropic titanium-based metal foams. Int J Mech Sci 2025;299:110431. http://dx.doi.org/10.1016/j.ijmecsci.2025.110431.
[70] Chao L, Li A, Liu S, Xu G, Deng Y. Compression and modeling of spherical aluminum foam composites. Int J Mech Sci 2025;308:111029. http://dx.doi.org/10.1016/j.ijmecsci.2025.111029.
[71] Du H, Weng P, Fang C, Zhang J, Weng GJ. Mechanical-thermal coupling of carbon fiber/aluminum/silicone foams under axial loading. Int J Mech Sci 2025;293:110201. http://dx.doi.org/10.1016/j.ijmecsci.2025.110201.
[72] Liu E, Bai Y, Su M, Li J, Hu Y, Ling R, Hao H. Mechanical enhancement of aluminum foam via in situ interfacial bonding. Int J Mech Sci 2024;265:108886. http://dx.doi.org/10.1016/j.ijmecsci.2023.108886.
[73] Karmakar P, Gupta S, Adlakha I. Low-rank approximation of local strain in two-phase composites. Int J Mech Sci 2024;264:108850. http://dx.doi.org/10.1016/j.ijmecsci.2023.108850.
[74] Rajput L, Jana P. Coupled nano-interfacial and agglomeration effects on elastic behavior of hybrid composites using multi-scale modeling. Int J Mech Sci 2025;296:110273. http://dx.doi.org/10.1016/j.ijmecsci.2025.110273.
[75] Jalali S, Pugno N. A dissolvable micromechanics model for composites. Int J Mech Sci 2024;266:108913. http://dx.doi.org/10.1016/j.ijmecsci.2023.108913.
[76] Betancourt-Tovar M, Cuan-Urquizo E, Roman-Flores A. Design and micromechanics characterization of additively manufactured architected cylindrical structures. Int J Mech Sci 2025;294:110199. http://dx.doi.org/10.1016/j.ijmecsci.2025.110199.
[77] Fathalian M, Darban H, Postek E. Atomistic insights into tensile damage of functionally graded al-SiC composites. Int J Mech Sci 2025;288:110012. http://dx.doi.org/10.1016/j.ijmecsci.2025.110012.
[78] Zhong Z, An J, Wu D, Gao N, Liu L, Wang Z, Meng F, Zhou X, Fan T. A machine learning strategy for enhancing the strength and toughness in metal matrix composites. Int J Mech Sci 2024;281:109550. http://dx.doi.org/10.1016/j.ijmecsci.2024.109550.
[79] Peng W, Le Ferrand H. Mechanical properties of template-based 3D graphene foams via multiscale modeling. Int J Mech Sci 2025;303:110621. http://dx.doi.org/10.1016/j.ijmecsci.2025.110621.
[80] Qin Z, Zhu L, Zhu J, Ying P, Busso EP, Li D, Sun L. High strain rate performance of Ni–co alloys with hierarchical nanotwins. Int J Mech Sci 2026;324:111741. http://dx.doi.org/10.1016/j.ijmecsci.2026.111741.
[81] Baishya MJ, Muthu N, Khanikar P. In pursuit of a high-performance mechanical metamaterial: Simple-cubic-octahedral plate lattice. Int J Mech Sci 2024;272:109189. http://dx.doi.org/10.1016/j.ijmecsci.2024.109189.
[82] Richert C, Huber N. A review of experimentally informed micromechanical modeling of nanoporous metals: From structural descriptors to predictive structure-property relationships. Materials 2020;13(15):3307. http://dx.doi.org/10.3390/ma13153307.
[83] Chang K. On the maximum strain criterion—a new approach to the angled crack problem. Eng Fract Mech 1981;14(1):107–24. http://dx.doi.org/10.1016/0013-7944(81)90021-7.
[84] Loh H-C, Divoux T, Gludovatz B, Gilbert PUPA, Ritchie RO, Ulm F-J, Masic A. Nacre toughening due to cooperative plastic deformation of stacks of co-oriented aragonite platelets. Commun Mater 2020;1:77. http://dx.doi.org/10.1038/s43246-020-00078-y.
[85] Launey ME, Buehler MJ, Ritchie RO. On the mechanistic origins of toughness in bone. Annu Rev Mater Res 2010;40:25–53. http://dx.doi.org/10.1146/annurev-matsci-070909-104427.
[86] Xiao Y, Zhang G, Huang K, Xue Y. Bioinspired cementitious composites with enhanced toughness and electromagnetic wave absorption. Int J Mech Sci 2025;286:109895. http://dx.doi.org/10.1016/j.ijmecsci.2024.109895.
[87] Meng Z, Xu Y, Zhou W, Bol RJ, Xie J, Šavija B. Confinement mechanisms governed by stiffness contrast in auxetic cementitious composites. Int J Mech Sci 2026;318:111546. http://dx.doi.org/10.1016/j.ijmecsci.2026.111546.